Enhancement of Cryogenic Pool Boiling Through Surface Modifications

Andrew Jacob

A thesis
submitted in partial fulfillment of the
requirements for the degree of

Master of Science

University of Washington
2024

Committee:
James Hermanson, Chair
Carl Knowlen

Program Authorized to Offer Degree:
Aeronautics & Astronautics

University of Washington

Abstract

Enhancement of Cryogenic Pool Boiling Through Surface Modifications

Andrew Jacob

Chair of the Supervisory Committee:
James Hermanson
Aeronautics & Astronautics

Cryogenic liquids are critical in many space systems, such as for propulsion, power generation, and for providing breathing air. Experiments were conducted to examine the pool boiling behavior of liquid nitrogen as a liquid-oxygen simulant. Cylindrical test specimens with different geometries and surface configurations (grooves) were heated by embedded electrical cartridge heaters. Multiple embedded thermocouple sensors were used, combined with corrections for variations in the thermal conductivity with temperature, corrections for surface area increase and fin effectiveness, to determine the rate of heat transfer in the nucleate boiling regime. The overall rates of heat transfer and boiling were within the comprehensive ranges of previously reported experiments. The rate of heat transfer for the grooved cylinders was seen to be higher by approximately a factor of ten for horizontal cylinders with smooth surfaces, and a factor of two for vertical cylinders. The heat flux increase was greater at the lower portion of the vertical cylinder compared with the middle section. Correcting the rates of heat flux for differences in surface area due to the addition of groves suggests a substantial decrease in the estimated amount of heat flux gain. Using a fin effectiveness correction for the grooved surfaces however suggests a 12-15% increase in the overall rate of heat transfer coefficient over the initial measured values.

Contents

List of Figures **iv**

Nomenclature **v**

Acknowledgements **vii**

1 Introduction **1**

1.1 Background 1

1.2 Previous Approaches 4

2 Experimental Apparatus **6**

2.1 Heater Geometry 6

2.2 Material Selection 7

2.3 Test Chamber Design 9

3 Test Procedure and Heat Flux Determination **14**

3.1 Analytical Solution 17

4 Results **20**

4.1 Surface Area Correction 24

4.2 Fin Efficiency Correction 25

5 Conclusions **27**

5.1 Future Work 28

A Appendix **33**

A.1 MATLAB Code For Insulation and Safety Calculations 34

A.2 MATLAB Code For Calibrating Data 36

A.3 MATLAB Code For Calculating Heat Transfer Coefficient 37

A.4 MATLAB Code For Calculating Tolerance Variations in Different Sensor Types 39

List of Figures

1.1 Typical boiling curve for water at 1 atm pressure [5] 3

2.1 Preliminary material internal temperature estimate for various materials at different wall superheat levels. 7

2.2 Experimental Configuration: (1), insulated container; (2), test surface (horizontal); (3), heater wire; (4), action camera; (5), mounting rods (light source not shown) 9

2.3 Heat flux accuracy comparison of different sensor types for various wall super heat levels. 10

2.4 Heat flux accuracy variation at 5.1 K wall super heat for different types of sensors. 11

2.5 Cost analysis based on tolerance for different sensor types. 11

2.6 Test apparatus with horizontal (left) and vertical (right) test cylinder orientations (the chamber shown is empty of liquid nitrogen). 13

3.1 Diagrams of smooth and grooved cylinders showing thermocouple wells and surface modifications. The cartridge heaters are embedded in the centers of each cylinder. 15

3.2 16

3.3 Heat flux profile comparison between variable and constant thermal conductivity. The horizontal scale reflects conditions near the exposed surface. . . . 17

3.4 Comparison of heat transfer coefficient calculations using composite (Eq. 3.4) and analytical (Eq. 3.10) solutions. 19

4.1 Uncorrected heat flux results comparing smooth and grooved cylinders . . . 21

4.2 Uncorrected convective heat transfer coefficient comparison between smooth and grooved cylinders 21

4.3 Uncorrected heat flux results comparison to historical data. Current results shown with solid symbols. 22

4.4 Convective heat transfer coefficients after surface area correction 24

4.5 Convective heat transfer coefficients after fin effectiveness correction 26

Nomenclature

A	=	Surface area of smooth cylinder	(m^2)
g	=	Gravitational acceleration	(m/s^2)
h	=	Convective heat transfer coefficient for smooth cylinder	($W/m^2\text{-}K$)
k	=	Thermal conductivity of cylinder	($W/m\text{-}K$)
L	=	Length of cylinder	(m)
Q	=	Heat flow	(W)
q	=	Heat flux	(W/m^2)
R_t	=	Total thermal resistance for radial conduction	(K/W)
r	=	Radial position in cylinder	(m)
r_{crit}	=	Critical bubble radius	(m)
T	=	Temperature	($^\circ$K)
t_b	=	Thickness of the space between fins	(m)
t_f	=	Thickness of the fin	(m)
ρ_l	=	Density of liquid	(kg/m^3)
σ	=	Surface tension	(N/m)

List of Subscripts

g	=	Grooved cylinder
f	=	Fin correction
b	=	Fin base
i	=	Inner cylinder location
o	=	Outer cylinder location
sur	=	Surface
∞	=	Ambient (LN_2 at 77.34 K)

Acknowledgements

Thank you to Professor James Hermanson for advising the research conducted. This author would also like to thank Mr. Andrew Jansen and Ms. Evelyn Madewell for helping to run experiments, and to the University of Washington A&A machine shop for providing access to machines and recommendations on manufacturing processes. This work was funded by Blue Origin Grant number 102R021 with the collaboration with Gary Grayson and Michael Friedman gratefully acknowledged.

Chapter 1

Introduction

1.1 Background

Cryogenic liquids play a critical role in many space systems. The high performance of liquid hydrogen and liquid oxygen as bipropellants points to their ongoing use for space-propulsion applications. At the same time, the use of these cryogens leads to substantial challenges in propellant storage. In addition to propulsion applications, cryogenic liquids may be used to provide breathing air for both the cabin and spacesuit environment [1]. Oxygen and hydrogen gas are also essential reactants for fuel cells that provide for space power and can also be used to power Reaction Control System (RCS) thrusters. The use of cryogenic liquids also has terrestrial applications in component cooling, such as high-power electronic circuits and enabling superconductivity [2]. These above applications point to an ongoing need to achieve highly-efficient heat transfer and boiling in compact cryogenic-fluid devices, with increasing demands to reduce the weight and to impact power consumption [3].

Pool boiling is known to be a stable and efficient method of producing vapor and trans-

ferring large quantities of heat [4]. A typical boiling curve for water is shown in Fig. 1.1 [5]. As the wall temperature is increased above the saturation temperature of the liquid, bubbles begin to form leading to the onset of nucleate boiling (ONB). A subsequent increase in the heat input causes vapor to escape from the surface in jets and columns, eventually leading to a maximum in heat flux termed the critical heat flux (CHF). A further increase in heat flux causes boiling to transition to film boiling, where the surface dries out and heat transfer to the liquid is primarily by radiation.

Improving cryogenic boiler design depends on an improved understanding of the boiling behavior and the accompanying heat flux. The rate of heat transfer in cryoboiling is strongly impacted by the dynamics of the vapor bubbles departing the heated surface [3, 6]. The bubble behavior starts with small, isolated bubbles at low heat flux, with larger bubbles merging into clusters as the CHF is approached. In addition, the number of active sites appears to be dependent on the surface temperature [3]. It can be noted that visualization studies to date have generally used smooth-wall surfaces [6]. Allowing a heated surface to cool upon exposure to a colder liquid, a minimum in heat flux (the Leidenfrost point, LFP) occurs as the boiling moves from pure film boiling into a transitional regime where both nucleate and film boiling occur. It should be noted that while the boiling characteristics of cryogenic liquids in flow-boiling configurations are also important and have been extensively studied [7], [8], there is still a large amount of uncertainty in the results. The experiments reported here are focused on the nucleate, pool boiling regime.

There have been many studies of the boiling behavior of cryogenic liquids for a variety of geometric configurations, test conditions, including some studies on the effects of surface materials and conditions [9]. These have led to different correlations [3] as well as theoretical

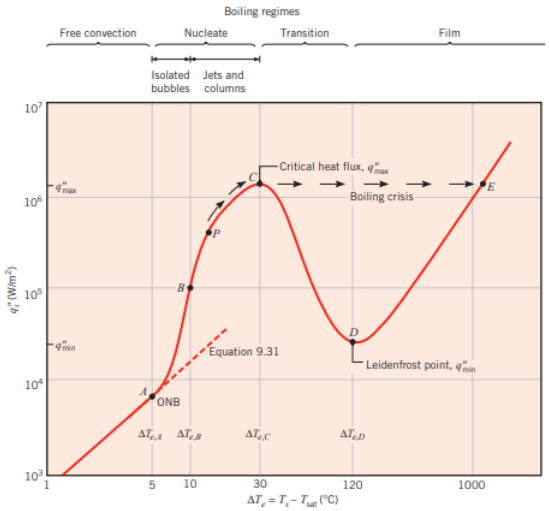

Figure 1.1: Typical boiling curve for water at 1 atm pressure [5]

.

models [2] to characterize the various boiling regimes as well as the ONB, CHF, and LFP. In spite of this, considerable uncertainly persists, with experimental results often differing by an order of magnitude or more for a given test configuration [10]. One topic of particular importance is the influence of the surface condition on the rate of boiling and vapor production.

Significant increases in the rates of heat transfer and boiling have been reported using porous coatings of different thicknesses [11], roughened surfaces [2], channels and grooves [12] and microstructured surfaces [4]. The wall material thermal conductivity has also been shown to influence pool boiling heat transfer [9, 13]. Easily characterized surface-modification approaches include drilling channels or making grooves [12]. Pool boiling experiments done here have precisely defined surface conditions, such as grooves of specified depth, width, and spacing, all of which have been seen to influence the boiling behavior [4]. However, comparatively few of these studies have involved cryogenic liquids. Establishing and quantifying these effects will have significant implications for cryogenic boiler design. Examining the

impact of the surface geometry and condition on the boiling rate is the focus of the work reported here. The method of modifying the surface geometry has the benefit of being a passive technique and not requiring any additional power.

An important practical consideration in choosing the scale of any geometric alteration of a surface is the size of vapor bubbles as they depart the heated surface [4]. This critical bubble radius depends on the balance between buoyancy and surface tension as $r_{crit} = \sqrt{3\sigma/\rho_l g}$ (the density of the vapor is neglected here), and is approximately 1.8 mm for the case of liquid nitrogen boiling at one atmosphere pressure. This suggests a suitable lower bound on the scale for the proposed surface modifications. It is also well established that adding fins to a surface can also increase the rate of heat transfer, though this has not been extensively investigated for the case of cryogenic boiling to the best knowledge of this author. This is another focus of this study, given the modification of the surfaces by adding straight-wall grooves results in a fin-like surface configuration. The addition of fins increases surface area, and also impacts the surface temperature distribution.

1.2 Previous Approaches

Many different approaches have been used to calculate heat flux for boiling. For example, Bland used the volume of vapor bubbles and an estimate of surface temperature [14], while a study by Surtaev used the power input to calculate flux [11]. This study used a similar approach to what Zhang did with thermocouples embedded at different radial locations along the cylinder; however, Zhang offset the thermocouples azimuthally, while this study did not [3].

Boiling studies not done in liquid nitrogen have used approaches like Zhao using input power and estimated surface temperature [15] similar to Chen whom looked at the boiling curve for methane [6]. Pioro looked at a variety of different liquids including water, ethanol, and benzene and calculated heat flux using bubble formation [16]. With all of the different approaches used, there is a large amount of uncertainty in the results. The objective of this work is to gain new estimates on the effects of grooves with experiments done with the same materials, overall dimensions, orientation and test conditions.

Chapter 2

Experimental Apparatus

2.1 Heater Geometry

There are several different types of geometries that have been studied for boiling, from plates to cylinders to wires [10]. Cylinders were chosen for the test specimen in this work due to the azimuthal symmetry resulting in the ability for one-dimensional analysis of heat transfer. The length and diameter of the cylinder were determined by insuring the length to diameter ratio is at least 10:1 so edge effects are minimized. Due to restrictions in commercial heater availability the internal diameter was chosen to be 0.64 cm and the outer diameter 2.5 cm. The overall length of the cylinder was 26.5 cm long resulting in a length to diameter ratio of 10.6:1. Thermocouples were placed as close as possible to the outside surface and the inside heater.

2.2 Material Selection

Determining the material used for the cylinders relied on a balance of insuring a sufficiently large difference in measured temperature between the thermocouples and achieving as wide of a range in surface temperatures as possible. An estimate of temperature difference for tests at different levels of wall superheat in the nucleate boiling regime between the materials was performed and is shown in Fig. 2.1. Copper was ruled out since the estimated difference in internal temperature ranged from 5 K at a 7 K wall superheat to 0.03 K at a wall superheat

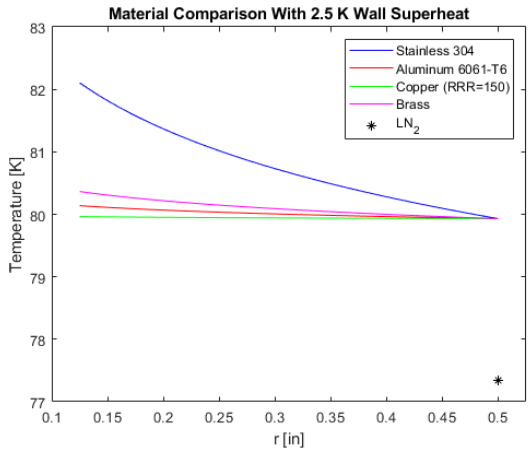

(a) Low level of wall superheat

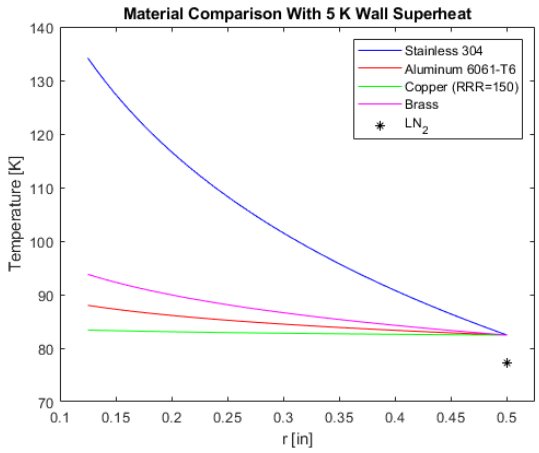

(b) Middle level of wall superheat

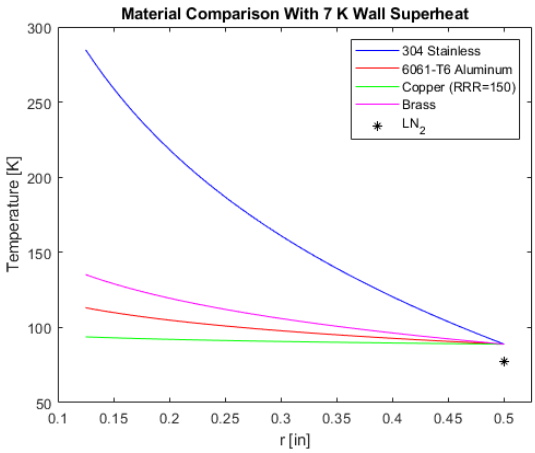

(c) High level of wall superheat

Figure 2.1: Preliminary material internal temperature estimate for various materials at different wall superheat levels.

of 2.5 K. With the thermocouple tolerance best case at 0.3 K for each thermocouple, the difference was deemed too low, especially at the middle and low range of wall superheat. Stainless steel 304 was originally selected due to the very low thermal conductivity resulting in an internal temperature difference of 2 K on the low end to 196 K on the high end. The low thermal conductivity of stainless steel would also be ideal for measuring the heat transfer coefficient at low wall temperatures. The downsides of stainless steel was measuring the higher end of the nucleate boiling regime since the heater is not powerful enough to achieve the wall temperatures needed. Another shortcoming of stainless steel is the machinability, especially compared to aluminum or brass. A stainless steel cylinder was made and preliminary tests were done to validate experimental design and set up, but given the difficulties with machining, stainless steel was not selected for further testing. The final material selected was aluminum due to cost, machinability and the desire to measure the boiling coefficient closer to the critical heat flux.

2.3 Test Chamber Design

Experiments were performed in this study using liquid nitrogen, a non-reactive cryogenic liquid for which there is a large, existing database of results [10], that is thermodynamically very similar to liquid oxygen. The configuration consists of an insulated vessel 34.3 cm in diameter fitted with a horizontal or vertical test specimen as shown in Fig. 2.2. The volume of liquid nitrogen is approximately 17 L. The test articles consist of cylinders with smooth surfaces and surfaces modified by the addition of square, straight-wall grooves. Heating is provided by embedded electrical heaters. All tests were performed at one atmosphere pressure.

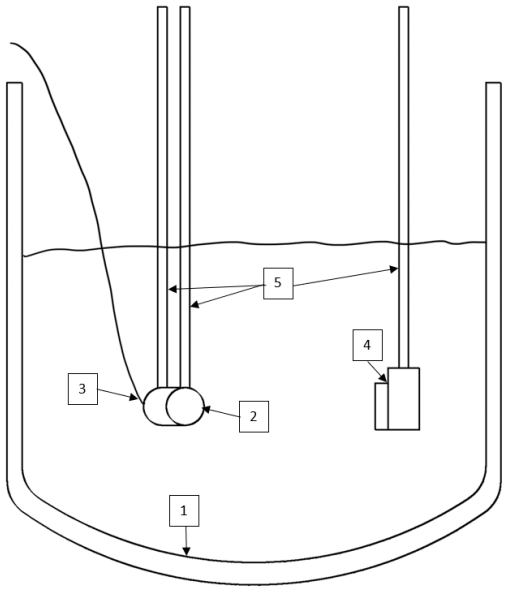

Figure 2.2: Experimental Configuration: (1), insulated container; (2), test surface (horizontal); (3), heater wire; (4), action camera; (5), mounting rods (light source not shown)

The test articles were fitted with multiple copper-constantan thermocouples to measure temperatures at multiple locations and to calculate heat flux using Fourier's law, taking into account variations in the thermal conductivity of the material at cryogenic temperatures.

Visualization is performed by a submerged camera in a waterproof case and connected to external power, as sketched in Fig. 2.2. Illumination is provided by a xenon arc lamp.

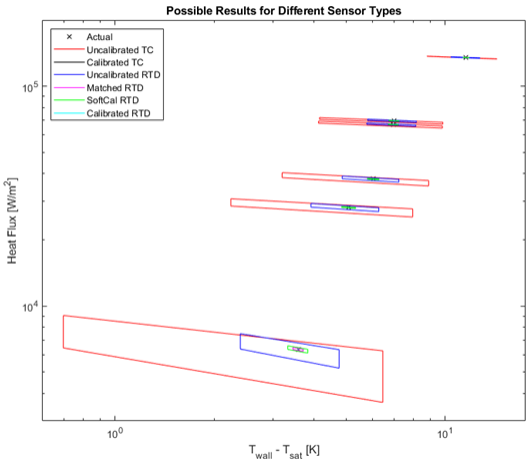

Figure 2.3: Heat flux accuracy comparison of different sensor types for various wall super heat levels.

The choice of sensors has an important impact on the experimental accuracy. Two different types of sensors were considered, thermocouples or RTDs. While RTDs are the industry standard, they come at the cost of high price so thermocouples were used. The variance for the two sensor types at different calibration levels for different levels of wall superheat are shown in Fig. 2.3. Since the temperature difference between the wall and the heater is greater at higher levels of heater input and wall superheat, the tolerance decreases. A closer look at the different sensors is shown in Fig. 2.4a and Fig. 2.4b at an intermediate level of wall superheat of 5.1 K. To determine the optimal sensor type for this study a cost analysis was done that evaluated the heat flux variation relative to cost by taking the diagonal length of the heat flux variation box plotted against the cost. The result is shown in fig. 2.5 and the closer to the bottom left the better. A calibrated thermocouple clearly provides the highest accuracy for the price so that was chosen for this study. Thermocouple calibration

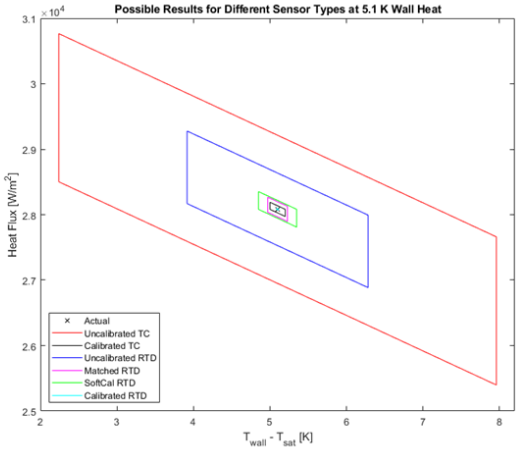

(a) Heat flux accuracy variation.

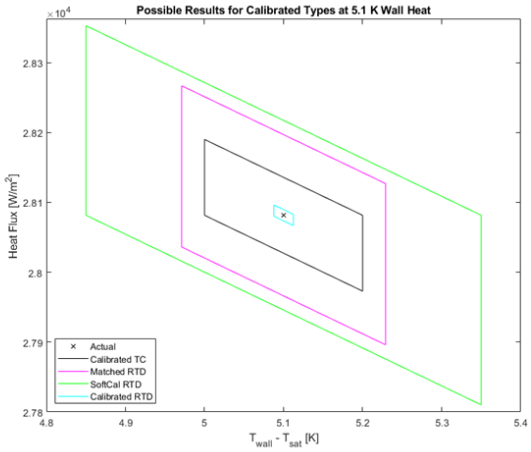

(b) Closer look on tighter tolerance sensor heat flux variation.

Figure 2.4: Heat flux accuracy variation at 5.1 K wall super heat for different types of sensors.

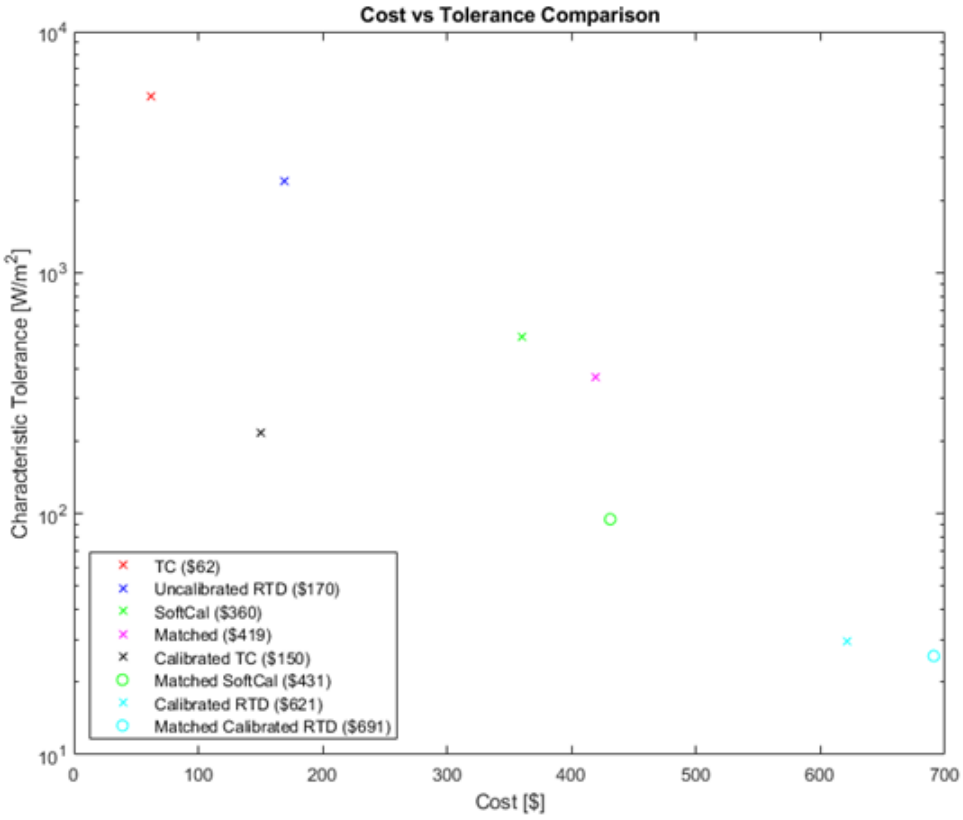

Figure 2.5: Cost analysis based on tolerance for different sensor types.

was done in ice water and liquid nitrogen temperature using a two-point calibration method as described in Appendix A.2, which decreases the accuracy to $\pm 0.3°C$. While a three-point calibration using dry ice would have resulted in a better calibration, the slight increase in accuracy was not deemed worthwhile given the difficulty of performing a calibration point with dry ice since it is a solid.

Different configurations for the actual experimental set-up are shown in Fig. 2.6. The action camera is shown on the left while the test cylinder is on the right of the figure. The lead wires coming from the cylinder were the embedded thermocouples and the wire coming from the end of the cylinder was from the cartridge heater. A grooved horizontally mounted cylinder is shown in Fig. 2.6a while Fig 2.6b illustrates how the experiment was configured with a smooth vertical cylinder. The length-to-diameter ratio of the cylinders was selected to be sufficient to minimize end effects. The grooves were 2 mm in width, depth and spacing and were made interior to the surface (thus all specimens had the same outer diameter). The outer thermocouple on the grooved cylinder was situated at the base of the fin. Figure 3.1a shows the outer thermocouple well moved in slightly when compared to the smooth cylinder shown in 3.1b as dictated by the presence of the groove. Each thermocouple well was packed with Apiezon N thermal grease to provide a seal from the liquid nitrogen. The groove spacing and cylinder material were chosen for manufacturing simplicity and for the availability of NIST data [17] on thermal conductivity at cryogenic temperatures.

The first step in the design of the test chamber was determining appropriate insulation and ensuring safety. For simplicity and cost-effectiveness, an open pot with side and bottom insulation was selected. The chosen method of insulation was an aerogel specially designed for cryogenic temperature called cryogel due to the thermal conductivity being 0.01 $^{W}/_{m-K}$.

(a) Horizontally mounted grooved cylinder (b) Vertically mounted smooth cylinder

Figure 2.6: Test apparatus with horizontal (left) and vertical (right) test cylinder orientations (the chamber shown is empty of liquid nitrogen).

A MATLAB code, shown in Appendix A.1, was developed to determine the thickness of the insulation needed to have adequate test duration. The determined thickness was 5 mm that would allow for a pot of liquid nitrogen to last for approximately two hours in the absence of external heat input. The safety calculations were carried out to assess the asphyxiation risk of boiling liquid nitrogen assuming worst case scenario of a sealed lab and all nitrogen boiling instantly. It was found that even in the worst case, the partial pressure of oxygen would not drop below unsafe levels and with the fume hood in the lab, asphyxiation risk was negated. The test chamber for this study had to have wide flexibility for mounting any type of heater design. The chosen design featured an overhead bar with vertical threaded rods where the heater could be mounted and suspended in the nitrogen. This would allow for both horizontal and vertical tests for plates and cylinders. Aluminum 8020 rail was used due to the flexibility and simplicity, which allows for adjustments in cylinder depth and horizontal location. 8020 rail also allows for additional sensors or anything else such as a camera to be easily added to the experiment setup.

Chapter 3

Test Procedure and Heat Flux Determination

Tests were conducted by first filling the test chamber with liquid nitrogen and letting the chamber cool down, then the test specimen was slowly lowered into the chamber allowing the thermal grease in the thermocouple wells to harden and form a seal. After the cylinder reached equilibrium temperature with the surrounding liquid nitrogen temperature, the desired input power was selected for the electric heater and applied for five minutes to allow the test specimen to come to a quasi-steady-state. After the five minute heating period, the heater was turned off and the specimen was allowed to cool for four minutes to return to ambient liquid nitrogen temperature. The test was repeated for various voltage settings and once completed, the temperature readings during the quasi-steady-state were averaged to get inner and outer values for calculating the convective heat transfer coefficient.

The cross sections shown in Fig. 3.1 indicate the radial positions of the inner and outer thermocouple wells. The bottom of the wells are sloped towards the center from the drill

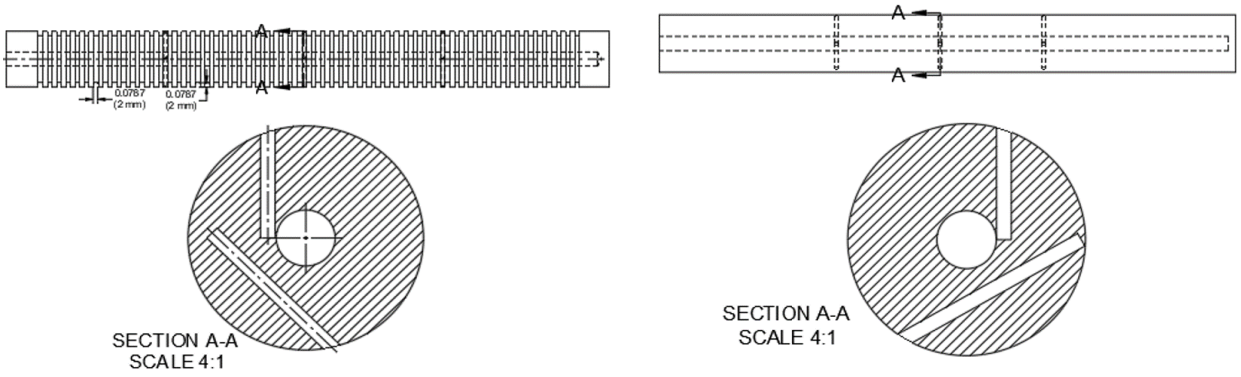

(a) Grooved cylinder geometry (b) Smooth cylinder geometry

Figure 3.1: Diagrams of smooth and grooved cylinders showing thermocouple wells and surface modifications. The cartridge heaters are embedded in the centers of each cylinder.

bit profile resulting in easy thermocouple centering in the wells from gentle pressure. These thermocouple readings were first used to generate a theoretical temperature profile shown in Fig. 3.2a. A composite technique is used to estimate the heat flux by using this temperature profile to calculate the thermal resistance of the cylinder by performing an average over 1000 radial elements where the thermal conductivity of each element is calculated from the temperature at the midpoint of the element using NIST data [17]. Once the thermal resistance is computed, the corrected heat flux is calculated as shown in Fig. 3.2b. The flux value at the outer most point of the cylinder is taken, with the extrapolated surface temperature to determine the convective heat transfer coefficient. The relevant equations are [5]:

$$Q = -k \cdot A \frac{dT}{dr} = h \cdot A(T_{sur} - T_{\infty}) \tag{3.1}$$

$$T(r) = \frac{T_i - T_{sur}}{ln(r_i/r_o)} ln\left(\frac{r}{r_o}\right) + T_{sur} \tag{3.2}$$

$$R_t = \sum_{n=1}^{1000} \frac{ln\left(r_{n+1}/r_n\right)}{2\pi L k_n} \tag{3.3}$$

$$Q = \frac{T_i - T_{sur}}{R_t} \tag{3.4}$$

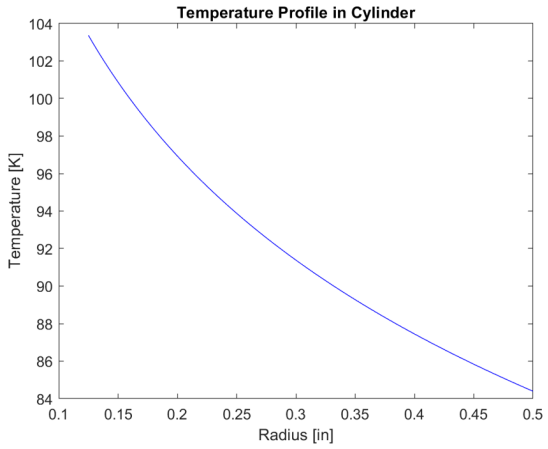

(a) Theoretical temperature profile through a test cylinder based on the thermocouple readings

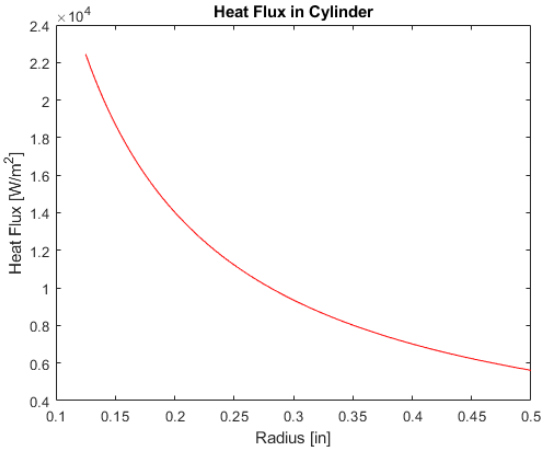

(b) Corrected heat flux throughout cylinder using the composite technique

Figure 3.2

Equation 3.1 was used to calculate the heat rate through the cylinder where the theoretical temperature profile, $T(r)$, is defined by Eq. 3.2. The thermal resistance for a composite cylinder was calculated with Eq. 3.3 with subscript n denoting the radial elements. The total heat flow and then the convective heat transfer coefficients were calculated with Eq. 3.4 in terms of the measured temperatures and known geometry. The comparison between the heat flux profile with the variable thermal conductivity and with a constant thermal

conductivity is shown in Fig. 3.3. The difference shows an overall decrease in heat flux of about 2% due to the non-uniform thermal conductivity. The stated uncertainty in the temperature measurement at each thermocouple was $\pm 0.3°C$ Combining this with the uncertainty in the thermocouple position and variations in the thermal conductivity suggest and overall uncertainty in the heat flux measurement of approximately 20%. The calculated theoretical temperature profile calculated from Eq. 3.2 is shown in Fig. 3.2a. The corrected heat flux profile shown in figure 3.2b was derived from Eq. 3.4 after dividing by the area of the cylinder at a given radial location.

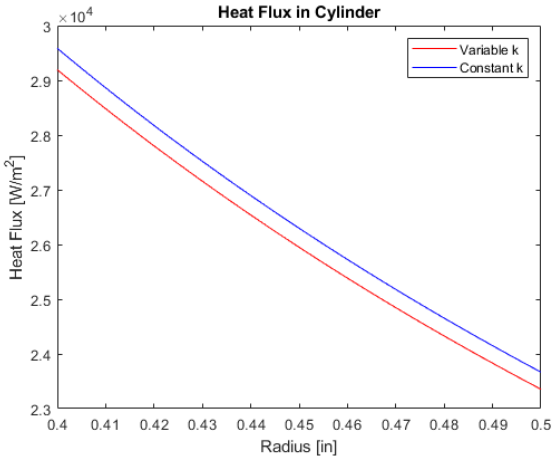

Figure 3.3: Heat flux profile comparison between variable and constant thermal conductivity. The horizontal scale reflects conditions near the exposed surface.

3.1 Analytical Solution

An analytical solution for solving for the heat flux can be obtained through integrating the convection heat equation shown in Eq. 3.5 where $k(T)$ is shown in Eq. 3.6. The remainder of the derivation is shown in Eq. 3.7 through Eq. 3.10.

$$-k(T)\frac{\partial T}{\partial r}2\pi rL = Q \tag{3.5}$$

$$k(T) = 10^{\left[0.07918+1.0957\cdot log(T)-0.07277\cdot log(T)^2+0.08084\cdot log(T)^3+0.02803\cdot log(T)^4-0.09464\cdot log(T)^5 \right.}$$
$$\left. +0.04179\cdot log(T)^6-0.00571\cdot log(T)^7\right] \tag{3.6}$$

$$-k(T)\frac{\partial T}{\partial r}2\pi r = \frac{Q}{L} \tag{3.7}$$

$$-k(T)\frac{dT}{dr}2\pi r = \frac{Q}{L} \tag{3.8}$$

$$-\int k(T)dT = \frac{Q}{2\pi L}\int \frac{r_o dr}{r} \tag{3.9}$$

$$q = \frac{-\int_{T_i}^{T_o} k(T)dT}{r_o \int_{r_i}^{r_o} \frac{dr}{r}} \tag{3.10}$$

A comparison between the composite and the analytical methods (Eq. 3.4 and Eq. 3.10 respectively) is shown in Fig. 3.4. This comparison was done with the grooved horizontal cylinder data. Given the large variance in previous studies, the difference between the two methods is not significant with the analytical solution being about a factor of 1.1 greater. The difference between the composite and analytical solution are likely due to a difference in boundary conditions. While the heat rate should be the same, this uses the assumption of radial heat transfer for the calculation of the heat rate while the composite solution only

makes the radial assumption when calculating the heat transfer coefficient h.

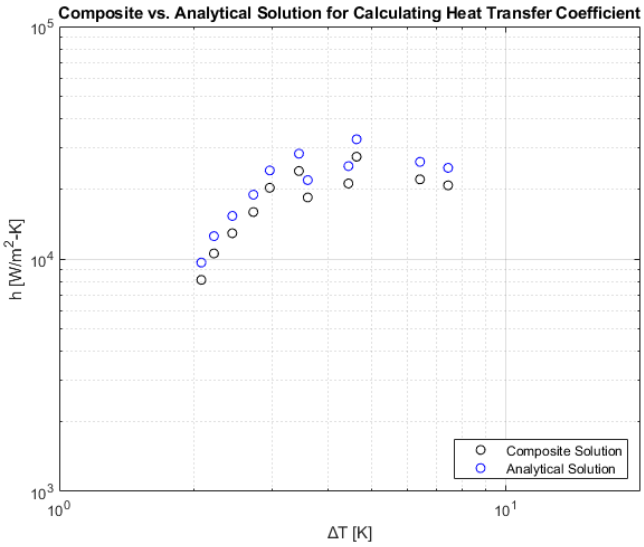

Figure 3.4: Comparison of heat transfer coefficient calculations using composite (Eq. 3.4) and analytical (Eq. 3.10) solutions.

Chapter 4

Results

Using the calculated heat flux value at the surface and the surface temperature, T_{sur}, the nucleate boiling curve can be plotted for different heater power inputs, with heat flux on the vertical axis and wall superheat, $T_{sur} - T_{\infty}$ on the horizontal axis. The observed differences between the horizontal and vertical tests between the smooth and grooved cylinders are shown in Fig. 4.1a and 4.1b respectively. The different datasets seen in the vertical test results are from two different thermocouple pairs, the lower set from the lowest thermocouple and the top set from the middle thermocouple pair. Results from the top thermocouple pair are not shown due to boil off causing the liquid level to fall below the sensor locations. The grooved surface modification of the cylinder is seen to have a significantly higher effect on the heat flux of horizontal cylinder than the vertical one. Figure 4.2 shows the corresponding convective heat transfer coefficients based on the superheating temperature. The horizontal case showed an increase heat transfer coefficient to be approximately factor of ten with the addition of grooves while the corresponding increase for the case of the vertical cylinder amounted to roughly a factor of two.

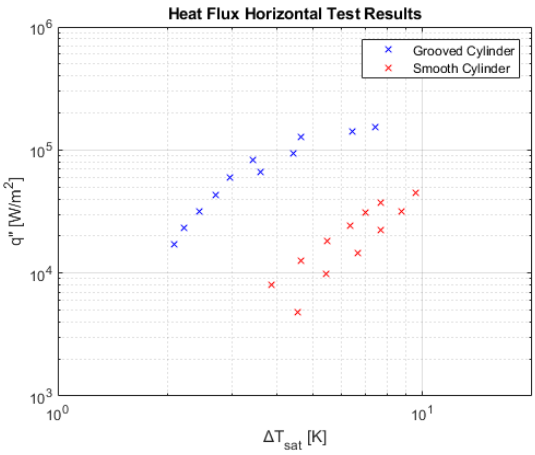

(a) Horizontal Cylinder

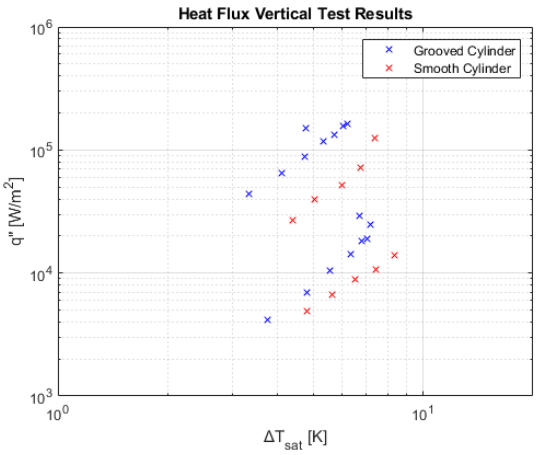

(b) Vertical Cylinder

Figure 4.1: Uncorrected heat flux results comparing smooth and grooved cylinders

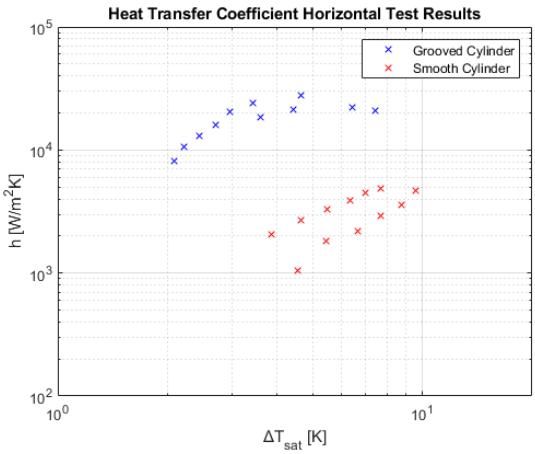

(a) Horizontal Cylinder

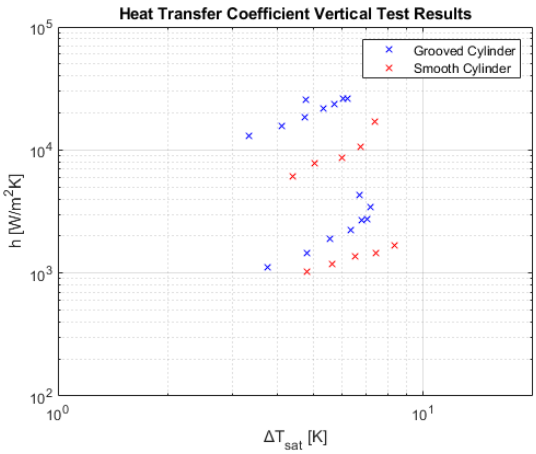

(b) Vertical Cylinder

Figure 4.2: Uncorrected convective heat transfer coefficient comparison between smooth and grooved cylinders

A comparison between the current results and previously published data for liquid nitrogen nucleate boiling is shown in Fig. 4.3 [10]. The lines are correlations and are largely for liquids other than liquid nitrogen so close agreement with cryogenic boiling results might not be expected. While the data from the literature are represented by the individual data points and shows a variation around two orders of magnitude. The isolated data points are measurements from experimental studies of cryogenic boiling; the solid lines and the

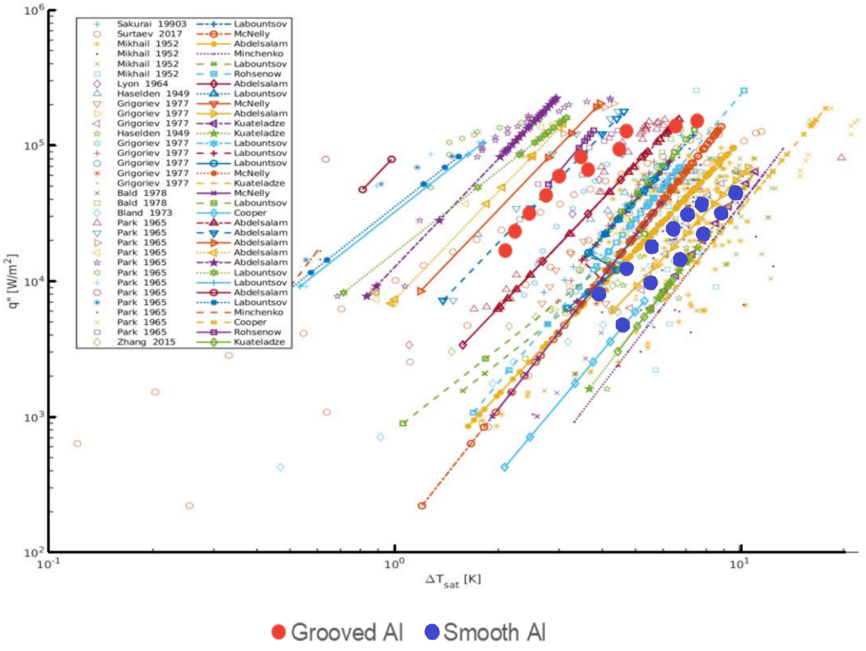

(a) Horizontal Cylinder. Historical measurements [18], [19], [20], [21],[22], [23], [24], [25], [11]. Correlations [26], [27], [28], [29], [30], [31]

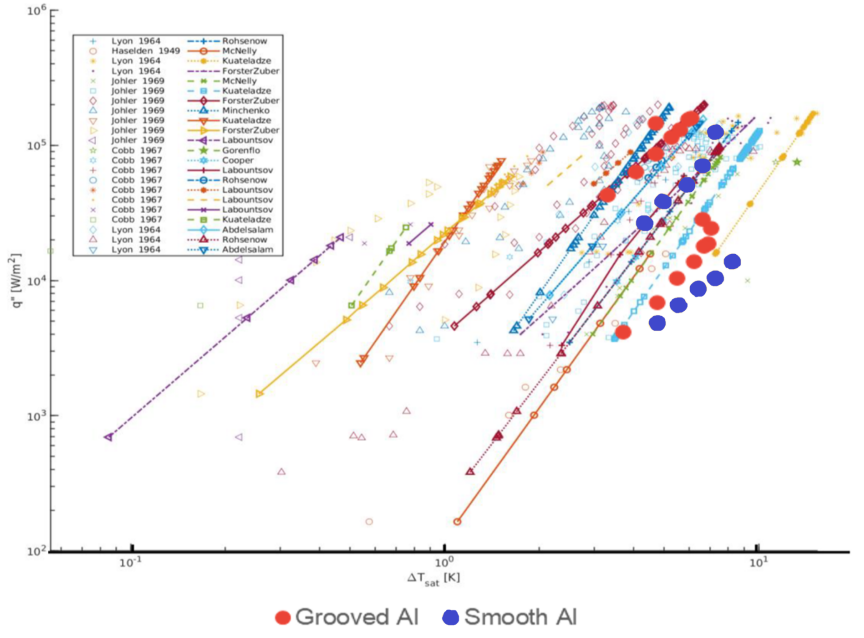

(b) Vertical Cylinder. Historical measurements [32], [33], [20], [21]. Correlations [27], [29], [34], [35], [36], [26], [37], [28]

Figure 4.3: Uncorrected heat flux results comparison to historical data. Current results shown with solid symbols.

points connected are from semi-empirical correlations, most of which were developed for non-cryogenic liquids.

The current results can be compared to those of previous studies. For example, Sathyabhama [12] reported an increase in the rate of heat transfer with increasing groove depth and decreasing channel width. The author attributed the improved heat transfer to improved bubble dynamics due to the larger heat transfer area and other considerations. Grooves and channels were seen to enhance the heat flux by as much as 2-3 times [12], with Sathyabhama *et al* [38] also showing significant increases with horizontal grooved cylinders.
Microstructuring on cylinders was also studied by Hossain [39] and others was seen to have a benefit ranging from 60-80% [40] up to a factor of 2 [41] in water and other liquids or up to a factor of 5 in the case of microchannels [42]. Surtaev [11] studied porous coatings and found a heat transfer enhancement of up to 300% using a technique of measuring power input and surface temperature to determine heat flux. This technique was impractical for this study due to the non-uniformities in the cartridge heaters employed.

4.1 Surface Area Correction

The results presented above did not explicitly take into account the increase in surface area for grooved cylinders. For the grooved cylinder, the convective heat transfer coefficient was, as a first approximation be adjusted based on Eqs. 4.1 and 4.2 where the area ratio is $A/A_g = 0.5205$ based on the fin geometry. This correction suggested the surface area corrected heat transfer coefficients, h_g and are shown in Fig. 4.4. The exposed area of the grooved cylinder is larger than that of the smooth cylinder which suggests a decrease in the actual heat transfer coefficient of about 50%, as seen in Fig. 4.4.

$$Q = A \cdot h \left(T_{sur} - T_{\infty}\right) = A_g \cdot h_g \left(T_{sur} - T_{\infty}\right) \tag{4.1}$$

$$h_g = \frac{A}{A_g} h_s \tag{4.2}$$

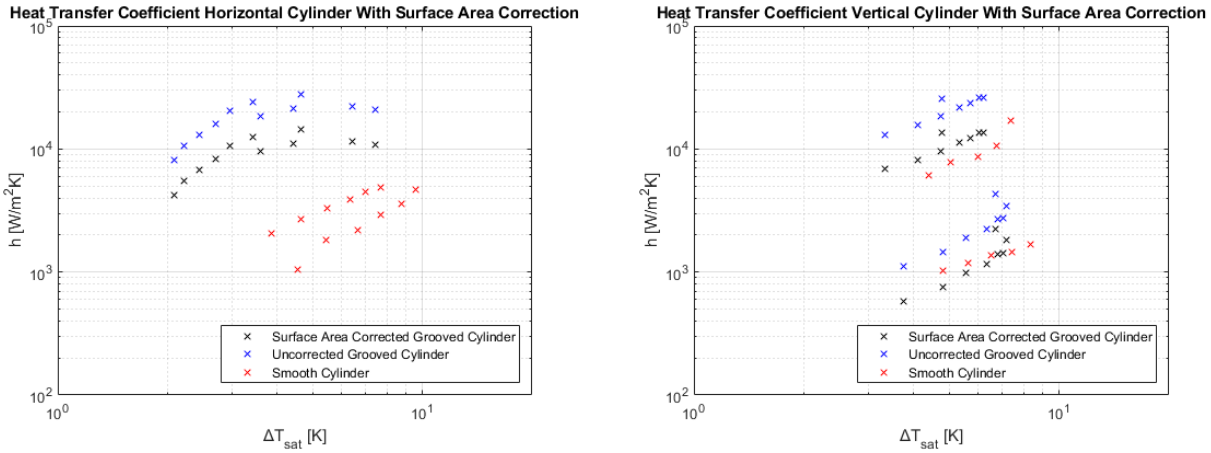

(a) Horizontal Cylinder (b) Vertical Cylinder

Figure 4.4: Convective heat transfer coefficients after surface area correction

4.2 Fin Efficiency Correction

A more complete accounting of the effects of grooves on the heat flux involves consideration of the actual grooved-surface geometry and heat transfer. The grooves effectively create a fin geometry, where the fins can be considered extensions on top of the underlying wall. The exposed area of each such fin, neglecting the tip regions, is given by $A_f = 2\pi(r_o^2 - r_i^2)$. The corresponding exposed area between each pair of fins is then $A_b = 2\pi r_i t_b$. Taking the base temperature of the fin to be equal to the temperature of the surface between the fins gives for the total heat flow for each fin/base combination of

$$Q = h(T_b - T_\infty)[\eta A_f + A_b] \tag{4.3}$$

This formulation takes an approximation that the heat transfer coefficient is constant over the fin/base region. Normalizing this heat flow by the corresponding heat flow in the absence of the fin, $Q_b = h(T_b - T_\infty)2\pi r_i(t_b + t_f)$ then gives

$$\frac{Q}{Q_b} = \frac{(\eta(r_o^2 - r_i^2) + r_i t_b)}{(r_i(t_b + t_f))} = \frac{h_f}{h} \tag{4.4}$$

where h_f would be the equivalent heat transfer coefficient in the presence of fins based on the temperature difference $T_b - T_\infty$ and the baseline heat transfer coefficient, h. The fin efficiency can be estimated using the formulation presented by Gardner [43], which takes into account the temperature decrease from the base region to the fin tip (heat transfer from the film tip is neglected in this analysis). An important note is that the heat transfer coefficient was assumed to have a uniform value on all surfaces regardless of wall superheat level. The

efficiency has estimated values ranging from 0.6 to 0.9 for the geometry and baseline heat transfer coefficient of this investigation. With the estimated efficiency values the corrected heat transfer coefficient could be calculated using the following equation:

$$h_f = h\frac{2\pi \cdot \eta(r_o^2 - r_b^2) + 2\pi r_b t_b}{2\pi r_i(t_b + t_f)} \tag{4.5}$$

The corrected heat transfer coefficients using this estimate of fin effectiveness are shown in Fig. 4.5 for the horizontal and vertical cylinders. The resulting heat transfer coefficients are seen to be roughly 15% higher and 12% higher for the horizontal and vertical cylinders, respectively. This analysis supports the overall conclusion that the heat transfer from the grooved cylinders substantially exceeds that of the corresponding smooth cylinders mounted in both horizontal and vertical configurations.

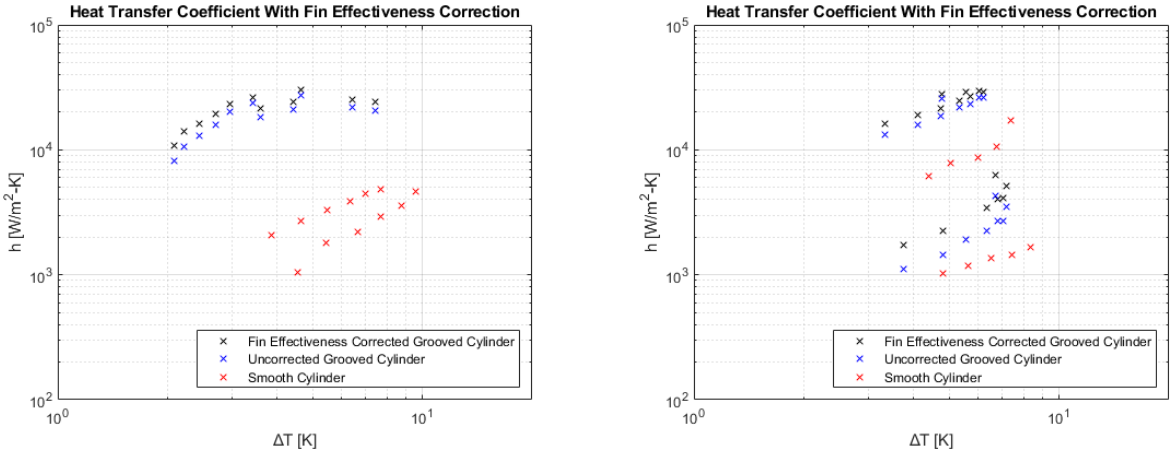

(a) Horizontal Cylinder (b) Vertical Cylinder

Figure 4.5: Convective heat transfer coefficients after fin effectiveness correction

Chapter 5

Conclusions

Experiments were conducted using liquid nitrogen to assess the impact of surface modifications on the rates of heat transfer and boiling in the nucleate boiling regime at one atmosphere pressure. Tests were done in both the horizontal and vertical orientations with both smooth and a grooved cylinders. Variations in the thermal conductivity were taken into account using the NIST database and averaging the results to get an effective thermal resistance within the cylinders. The grooved surfaces were shown to provide an increase in the heat transfer coefficient, with a larger increase for the horizontal case (about an order of magnitude compared to a factor of two for the vertical case). Correcting for the change in surface area alone suggested the heat transfer coefficient was substantially lower for the case of grooved vs. smooth cylinders with the horizontal case showing a factor of five increase and no increase for the vertical case. However a more complete analysis considering the fin effectiveness of the grooved cylinders, suggests that the heat transfer coefficients were somewhat higher (approximately 12-15% greater than baseline measurements) for the grooved cylinders. This study also found a higher heat transfer coefficient for the middle of the cylin-

der compared to lower down in the vertical case, while no axial difference was found in the horizontal case. Future work on this topic will include more complicated groove structures, different material variations and looking at different geometries other than cylinders.

5.1 Future Work

Future work on liquid nitrogen boiling from this study can follow many different routes from quenching studies, different fin design, and imaging. The main issue encountered in this study for quenching was estimating the derivative temperature difference between the two thermocouples of the with the noise variations. Using better smoothing algorithms or data acquisition could result in measuring the quenching boiling curve. Different fin geometries is the largest area of future study. Fins with spacing the same size or larger than the bubble diameter will be of interest in future studies. Imaging would provide valuable information on surface wetting, bubble size and bubble departure rate leading to more informed future fin designs.

Bibliography

[1] James L Yanosy. "Cryogenics and ECLSS–Past, Present, and Future Challenges". In: *SAE transactions* (2000), pp. 469–477.

[2] V Drach, N Sack, and J Fricke. "Transient heat transfer from surfaces of defined roughness into liquid nitrogen". In: *International journal of heat and mass transfer* 39.9 (1996), pp. 1953–1961.

[3] Xiaobin Zhang et al. "Visualization study of nucleate pool boiling of liquid nitrogen with quasi-steady heat input". In: *Cryogenics* 72 (2015), pp. 14–21.

[4] Jeet S Mehta and Satish G Kandlikar. "Heat transfer enhancement during pool boiling of water over horizontal and vertical tubes with micro structured surfaces". In: *International Conference on Nanochannels, Microchannels, and Minichannels*. Vol. 44793. American Society of Mechanical Engineers. 2012, pp. 71–80.

[5] Theodore L Bergman et al. *Introduction to heat transfer*. John Wiley & Sons, 2011.

[6] Hanzhi Chen et al. "Experimental investigations on bubble departure diameter and frequency of methane saturated nucleate pool boiling at four different pressures". In: *International Journal of Heat and Mass Transfer* 112 (2017), pp. 662–675.

[7] Mariano Mercado, Nathaniel Wong, and Jason Hartwig. "Assessment of two-phase heat transfer coefficient and critical heat flux correlations for cryogenic flow boiling in pipe heating experiments". In: *International Journal of Heat and Mass Transfer* 133 (2019), pp. 295–315.

[8] Jason Hartwig, Samuel Darr, and Anthony Asencio. "Assessment of existing two phase heat transfer coefficient and critical heat flux correlations for cryogenic flow boiling in pipe quenching experiments". In: *International Journal of Heat and Mass Transfer* 93 (2016), pp. 441–463.

[9] Cristiano Bombardieri and Chiara Manfletti. "Influence of wall material on nucleate pool boiling of liquid nitrogen". In: *International Journal of Heat and Mass Transfer* 94 (2016), pp. 1–8.

[10] R.C. Moore and J.C. Hermanson. "Evaluating the Complete Pool Boiling Curve for Liquid Nitrogen". In: *Final Report, NASA Grant and Cooperative Agreement Number 80NSSC19K1630* (January 19, 2022).

[11] AS Surtaev et al. "Heat transfer and crisis phenomena at pool boiling of liquid nitrogen on the surfaces with capillary-porous coatings". In: *International Journal of Heat and Mass Transfer* 108 (2017), pp. 146–155.

[12] Alangar Sathyabhama. "Nucleate pool boiling heat transfer from a flat-plate grooved surface". In: *Journal of Enhanced Heat Transfer* 22.3 (2015).

[13] I Gogonin. "Influence of the thickness of a wall and of its thermophysical characteristics on the critical heat flux in boiling." In: *Journal of Engineering Physics & Thermophysics* 82.6 (2009).

[14] ME Bland, CA Bailey, and G Davey. "Boiling from metal surfaces immersed in liquid nitrogen and liquid hydrogen". In: *Cryogenics* 13.11 (1973), pp. 651–657.

[15] Ch Zhao et al. "An experimental investigation on the entire pool boiling curve of R14 under 0.1 MPa pressure". In: *International journal of refrigeration* 41 (2014), pp. 164–170.

[16] IL Pioro, W Rohsenow, and SS Doerffer. "Nucleate pool-boiling heat transfer. I: review of parametric effects of boiling surface". In: *International Journal of Heat and Mass Transfer* 47.23 (2004), pp. 5033–5044.

[17] ED Marquardt, JP Le, and Ray Radebaugh. "Cryogenic material properties database". In: *Cryocoolers 11* (2002), pp. 681–687.

[18] A Sakurai, M Shiotsu, and K Hata. "A general correlation for pool film boiling heat transfer from a horizontal cylinder to subcooled liquid: Part 2—Experimental data for various liquids and its correlation". In: *Journal of Heat Transfer* 112 (May 1990), pp. 441–450.

[19] Nassif Rizk Mikhail. "Studies in Heat Transfer to Boiling Liquids at Low Temperatures". PhD thesis. University of London, 1952.

[20] David N Lyon. "Peak nucleate-boiling heat fluxes and nucleate-boiling heat-transfer coefficients for liquid N2, liquid O2 and their mixtures in pool boiling at atmospheric pressure". In: *International Journal of Heat and Mass Transfer* 7.10 (1964), pp. 1097–1116.

[21] GG Haselden, JI Peters, et al. "Heat transfer to boiling liquid oxygen and liquid nitrogen". In: *Trans Inst Chem Eng* 27 (1949), pp. 201–208.

[22] VA Grigoriev et al. "Concerning the influence of thermal properties of heating surface material on heat transfer intensity of nucleate pool boiling of liquids including cryogenic ones". In: *Cryogenics* 17.2 (1977), pp. 94–96.

[23] Efton Lilborn Park Jr. *Nucleate and film boiling heat transfer to methane and nitrogen from atmospheric pressure to the critical pressure.* The University of Oklahoma, 1965.

[24] Zhang Xiaobin et al. “CFD simulations and experimental verification on nucleate pool boiling of liquid nitrogen”. In: *Physics Procedia* 67 (2015), pp. 569–575.

[25] JR Thome and WB Bald. “Nucleate pool boiling in cryogenic binary mixtures”. In: *Proceedings of the 7th International Cryogenic Engineering Conference, London, S.* 1978, pp. 523–530.

[26] DA Labountzov. “Generalized correlation for nucleate boiling”. In: *Teploenergetika* 7.5 (1960), pp. 76–80.

[27] MJ McNelly. “A correlation of rates of heat transfer to nucleate boiling of liquids”. In: *J. Imperial College Chem. Eng. Soc* 7 (1953), pp. 18–34.

[28] K Stephan and M Abdelsalam. “Heat-transfer correlations for natural convection boiling”. In: *International Journal of Heat and Mass Transfer* 23.1 (1980), pp. 73–87.

[29] Warren M Rohsenow. “A method of correlating heat-transfer data for surface boiling of liquids”. In: *Transactions of the American Society of Mechanical Engineers* 74.6 (1952), pp. 969–975.

[30] MG Cooper. “Heat flow rates in saturated nucleate pool boiling-a wide-ranging examination using reduced properties”. In: *Advances in heat transfer*. Vol. 16. Elsevier, 1984, pp. 157–239.

[31] VM Borishansky, BI Bodrovich, and FP Minchenko. “Heat transfer during nucleate boiling of water and ethyl alcohol, in a volume of collection of articles”. In: *Aspects of heat transfer and hydraulics of two-phase mixtures, Govt. Energy Publishing House, Moscow* (1961), pp. 75–93.

[32] Craig Bauer Johler. “A study of the nucleate boiling of liquid nitrogen, liquid argon, and liquid carbon monoxide from atmospheric to near the critical pressure”. MA thesis. University of Missouri–Rolla, 1969.

[33] C. Cobb. “A study of surface and geometric effects on the nucleate boiling of liquid nitrogen and liquid argon from atmospheric to the critical pressure”. PhD thesis. niversity of Missouri–Rolla, 1967.

[34] SS Kutateladze. “On the transition to film boiling under natural convection”. In: *Kotloturbostroenie* 3 (1948), p. 10.

[35] Samson Semenovich Kutateladze. *Heat transfer in condensation and boiling*. Vol. 3770. US Atomic Energy Commission, Technical Information Service, 1959.

[36] HK Forster and Novak Zuber. “Dynamics of vapor bubbles and boiling heat transfer”. In: *AIChE Journal* 1.4 (1955), pp. 531–535.

[37] Dieter Gorenflo and David Kenning. “H2 pool boiling”. In: *VDI heat atlas*. Springer, 2009, pp. 757–792.

[38] A Sathyabhama and SP Prashanth. "Experimental investigation on boiling heat transfer coefficient enhancement using grooves for cooling of electronic devices". In: *Fourteenth Intersociety Conference on Thermal and Thermomechanical Phenomena in Electronic Systems (ITherm)*. IEEE. 2014, pp. 466–472.

[39] Md. Rakib Hossain, Md. Imran Hossain Talukder, and Md. Ashiqur Rahman. "Study of pool boiling on flat and micro-grooved brass and copper surfaces". In: *AIP Conference Proceedings* 2121.1 (2019), p. 030012.

[40] Balkrushna A Shah et al. "Experimental investigation of nucleate boiling over a smooth and micro-grooved cylindrical surface". In: *Technologies for Sustainable Development*. CRC Press, 2020, pp. 323–328.

[41] Houli Liu et al. "Enhancement of pool boiling heat transfer using 3D-printed groove structure". In: *International Journal of Heat and Mass Transfer* 183 (2022), p. 122155.

[42] Rajesh Kumar and B Premachandran. "Enhancement of Pool Boiling Performance Through an Asymmetric Dual V-Groove Microchannel Structured Surface". In: *Available at SSRN 4584051* (2023).

[43] Karl A Gardner. "Efficiency of extended surface". In: *Transactions of the American Society of Mechanical Engineers* 67.8 (1945), pp. 621–628.

Appendix A

Appendix

A.1 MATLAB Code For Insulation and Safety Calculations

```
clear, clc, close all

%% ----- Heat Transfer Inputs -----
k = 0.01;     % [W/mK] Thermal conductivity
x = 0.010;    % [m] Thickness of Insulation
d = 0.3084;   % [m] Diameter of pot
V_LN2 = 16.6;   % [L] Starting volume of LN2
T_N2 = 77;    % [K] Temperature of LN2
T_sur = 300;  % [K] Ambient temperature
hf = 1.992e5; % [J/kg] Enthalpy of vaporization
rho = 0.8084; % [kg/L] Density

%% ----- Heat Transfer Through Wall -----
% Geometry of LN2
h = (V_LN2*0.001)/(pi/4*d^2); % [m]
A = pi/4*d^2 + pi*d*h;        % [m^2]

% Calculate Heat of formation
Hf = hf*V_LN2*rho; % [J]

% Calculate Heat Rate
q = k*(T_sur-T_N2)/x*A; % [W]

% Calculate Time
Time = Hf/q/60; % [min]

fprintf('It takes %1.0f minutes for %1.0f L of LN2 to completely boil.\n',Time,↙
V_LN2)


%% ----- Dilution Inputs -----
Room_L = 25;           % [ft] Room Length
Room_H = 12;           % [ft] Room Height
O2_con = 0.21;         % Starting fraction of air that is O2
N2_con = 0.79;         % Starting fraction of air that is N2
Mm_N2 = 28.0134;       % [g/mol] Molar mass of N2
Mm_O2 = 31.9988;       % [g/mol] Molar mass of O2
V_mol_N2 = 0.02239329; % [m^3/mol] Density per mole at 1 atm of N2
V_mol_O2 = 0.02239344; % [m^3/mol] Density per mole at 1 atm of O2

%% ----- Dilution -----
% Volume of Room
V_room = 0.3048^3*Room_L^2*Room_H; % [m^3]

% Volume of N2 and O2 in the room
V_N2 = V_room*N2_con; % [m^3]
V_O2 = V_room*O2_con; % [m^3]

% Calculate moles of gas in the room
mol_N2 = V_N2/V_mol_N2; % [mol]
mol_O2 = V_O2/V_mol_O2; % [mol]

% Calculate moles of LN2
mass_LN2 = V_LN2*rho*1000; % [g]
```

```
mol_LN2 = mass_LN2/Mm_N2;  % [mol]

% Find new concentration of O2 and N2
new_mol_N2 = mol_LN2+mol_N2;   % [mol]
total_mol = new_mol_N2+mol_O2; % [mol]
x_N2 = new_mol_N2/total_mol;
x_O2 = mol_O2/total_mol;

fprintf('The O2 concentration dropped from %1.2f to %1.3f.\n',O2_con,x_O2)
fprintf('The N2 concentration rose from %1.2f to %1.3f.\n',N2_con,x_N2)
```

A.2 MATLAB Code For Calibrating Data

```
clear, clc

cal_fact = [-2.1869, -0.1515; % Channel 0
            -2.1373, -0.0079; % Channel 1
            -2.1471, 0.0041;  % Channel 2
            -5.4681, 0.0980;  % Channel 4
            -2.0486, -0.0031; % Channel 5
            -1.9940,-0.2969]; % Channel 6

Names = {'CH0' 'CH1' 'CH2' 'CH4' 'CH5' 'CH6'};
for i=1:6
    m(i) = (cal_fact(i,2)-cal_fact(i,1))/(273.15-77.34);
    b(i) = cal_fact(i,1)-(m(i)*77.34);
end

%%
celldata=tdmsread("C:↙
\Users\andre\Documents\School\Masters\Thesis\Data\NewDAQ\Al_Smooth_6923.tdms");

data = table2array(celldata{1,1});
t = 0.001:0.001:(length(data)-424999)/1000;
for i=1:6
    TC.(Names{i}) = data(425000:end,i);
end

for i=1:6
    TCcal.(Names{i}) = b(i)+m(i).*TC.(Names{i})+TC.(Names{i});
end

figure(2)
plot(t,TCcal.CH0,t,TCcal.CH1,t,TCcal.CH2,t,TCcal.CH4,t,TCcal.CH5,t,TCcal.CH6)
title('Smooth Al Cylinder'),xlabel('Time [s]'),ylabel('Temperature [K]'),legend↙
(Names)
```

A.3 MATLAB Code For Calculating Heat Transfer Coefficient

```
clear, clc

T_i = 83.1;  % [K]
T_o = 79.8;   % [K]

r_i = 0.15; % [in]  Smooth SS = 0.1665; Smooth Al = 0.175; Ribbed Al = 0.15;
r_o = 0.39243; % [in] Smooth SS = 0.47011; Else = 0.39243
R_o = 0.5; % [in] SS = 0.5; Else = 0.42126;
T_LN2 = 77.34;

Resolution = 1000;

r_i = r_i/39.37; r_o = r_o/39.37;

% Al
a_SS=0.07918;b_SS=1.0957;c_SS=-0.07277;d_SS=0.08084;e_SS=0.02803;f_SS=-0.09464;↙
g_SS=0.04179;h_SS=-0.00571;i_SS=0;
% SS
%a_SS=-1.4087;b_SS=1.3982;c_SS=0.2543;d_SS=-0.6260;e_SS=0.2334;f_SS=0.4256;g_SS=-↙
0.4658;h_SS=0.1650;i_SS=-0.0199;
k_fun = @(R) 10.^(a_SS+b_SS.*log10((T_i-T_o)/(log(r_i/r_o))*log(R/r_o)+T_o)+c_SS.*↙
(log10((T_i-T_o)/(log(r_i/r_o))*log(R/r_o)+T_o)).^2+d_SS.*(log10((T_i-T_o)/(log↙
(r_i/r_o))*log(R/r_o)+T_o)).^3+e_SS.*(log10((T_i-T_o)/(log(r_i/r_o))*log(R/r_o)↙
+T_o)).^4+f_SS.*(log10((T_i-T_o)/(log(r_i/r_o))*log(R/r_o)+T_o)).^5+g_SS.*(log10↙
((T_i-T_o)/(log(r_i/r_o))*log(R/r_o)+T_o)).^6+h_SS.*(log10((T_i-T_o)/(log(r_i/r_o))↙
*log(R/r_o)+T_o)).^7+i_SS.*(log10((T_i-T_o)/(log(r_i/r_o))*log(R/r_o)+T_o)).^8);

r = linspace(0.125,R_o,Resolution);
r = r./39.37;
Temp = (T_i-T_o)/(log(r_i/r_o))*log(r/r_o)+T_o;
TempGrad = Temp(1)-Temp(end)
WallHeat = Temp(end)-T_LN2

figure(19)
plot(r*39.37,Temp,'b')
title('Temperature Profile in Cylinder')
xlabel('Radius [in]'), ylabel('Temperature [K]')

R = 0;
for i=1:Resolution-1
    r1 = r(i); r2 = r(i+1); rmid = (r1+r2)/2;
    k = k_fun(rmid);
    R = R + log(r2/r1)/(k);
end
k_high = k_fun(r_i); k_low = k_fun(r_o);

R_high = log(r(end)/r(1))/k_high; R_low = log(r(end)/r(1))/k_low;
q_rate_high = (Temp(1)-Temp(end))/R_high;
q_rate_low = (Temp(1)-Temp(end))/R_low;
q_flux_high = q_rate_high./r; q_flux_low = q_rate_low./r;

q_rate = (Temp(1)-Temp(end))/R;

q_flux = q_rate./r;
```

```
figure(20)
plot(r*39.37,q_flux,'r',r*39.37,q_flux_high,'b')%,r*39.37,q_flux_low,'g')
title('Heat Flux in Cylinder'), legend('Variable k','Constant k')%,'Low')
xlabel('Radius [in]'), ylabel('Heat Flux [W/m^2]'), xlim([0.4 0.5])

q_s_flux = q_rate/(0.5/39.37)
q_s_flux_high = q_rate_high/(0.5/39.37)
q_s_flux_low = q_rate_low/(0.5/39.37)

h = q_s_flux/(WallHeat)
h_high = q_s_flux_high/(WallHeat)
h_low = q_s_flux_low/(WallHeat)
```

A.4 MATLAB Code For Calculating Tolerance Variations in Different Sensor Types

```
clear, clc, close all
WallSupHeat = [3.58,5.1,6.05,6.96,6.99,11.56];
k =↙
[8.55654774172104,9.55713373857111,9.90582745787569,10.6919023243577,10.754092987631↙
9,12.1310868302404];
T1 =↙
[93.9876685526912,134.171248931800,150.572897705039,194.462195732425,198.27504154812↙
3,284.826904832651];
T_LN2 = 77.34;
T2 = T_LN2 + WallSupHeat;

r1 = 0.125/39.37; r2 = 0.5/39.37;

for i = 1:length(k)
h(i) = 1/(r2*(T2(i)-T_LN2))*((k(i)*(T1(i)-T2(i)))/(log(r2/r1)));
q(i) = h(i)*(WallSupHeat(i));
end
%% --- Type T TC ---

tol_TC = 1.5/100;

limTC = 1;
for i = limTC:length(k)

T1_C(i) = T1(i)-273.15;
T2_C(i) = T2(i)-273.15;

tol_T1_TC(i) = abs(tol_TC*T1_C(i));
tol_T2_TC(i) = abs(tol_TC*T2_C(i));

T1_l(i) = T1(i)-tol_T1_TC(i); T1_h(i) = T1(i)+tol_T1_TC(i);
T2_l(i) = T2(i)-tol_T2_TC(i); T2_h(i) = T2(i)+tol_T2_TC(i);

WallSupHeat_h(i) = T2_h(i)-T_LN2;
WallSupHeat_l(i) = T2_l(i)-T_LN2;

% T1 high T2 high
h_hh(i) = 1/(r2*(T2_h(i)-T_LN2))*((k(i)*(T1_h(i)-T2_h(i)))/(log(r2/r1)));

% T1 hgih T2 low
h_hl(i) = 1/(r2*(T2_l(i)-T_LN2))*((k(i)*(T1_h(i)-T2_l(i)))/(log(r2/r1)));

% T1 low T2 high
h_lh(i) = 1/(r2*(T2_h(i)-T_LN2))*((k(i)*(T1_l(i)-T2_h(i)))/(log(r2/r1)));

% T1 low T2 low
h_ll(i) = 1/(r2*(T2_l(i)-T_LN2))*((k(i)*(T1_l(i)-T2_l(i)))/(log(r2/r1)));


q_hh(i) = h_hh(i)*(WallSupHeat_h(i));
q_hl(i) = h_hl(i)*(WallSupHeat_l(i));
q_lh(i) = h_lh(i)*(WallSupHeat_h(i));
q_ll(i) = h_ll(i)*(WallSupHeat_l(i));
```

```
q_lim_TC(:,i) = [q_hh(i);q_hl(i);q_ll(i);q_lh(i);q_hh(i)];
WallSupHeat_lim_TC(:,i) = [WallSupHeat_h(i);WallSupHeat_l(i);WallSupHeat_l(i);↙
WallSupHeat_h(i);WallSupHeat_h(i)];
end

%% --- Calibrated Thermocouples ---
tol_TCC = 0.1;

limTCC = 1;
for i = limTCC:length(k)

tol_T1_TCC(i) = tol_TCC;
tol_T2_TCC(i) = tol_TCC;

T1_l(i) = T1(i)-tol_T1_TCC(i); T1_h(i) = T1(i)+tol_T1_TCC(i);
T2_l(i) = T2(i)-tol_T2_TCC(i); T2_h(i) = T2(i)+tol_T2_TCC(i);

WallSupHeat_h(i) = T2_h(i)-T_LN2;
WallSupHeat_l(i) = T2_l(i)-T_LN2;

% T1 high T2 high
h_hh(i) = 1/(r2*(T2_h(i)-T_LN2))*((k(i)*(T1_h(i)-T2_h(i)))/(log(r2/r1)));

% T1 hgih T2 low
h_hl(i) = 1/(r2*(T2_l(i)-T_LN2))*((k(i)*(T1_h(i)-T2_l(i)))/(log(r2/r1)));

% T1 low T2 high
h_lh(i) = 1/(r2*(T2_h(i)-T_LN2))*((k(i)*(T1_l(i)-T2_h(i)))/(log(r2/r1)));

% T1 low T2 low
h_ll(i) = 1/(r2*(T2_l(i)-T_LN2))*((k(i)*(T1_l(i)-T2_l(i)))/(log(r2/r1)));

q(i) = h(i)*(WallSupHeat(i));
q_hh(i) = h_hh(i)*(WallSupHeat_h(i));
q_hl(i) = h_hl(i)*(WallSupHeat_l(i));
q_lh(i) = h_lh(i)*(WallSupHeat_h(i));
q_ll(i) = h_ll(i)*(WallSupHeat_l(i));

q_lim_TCC(:,i) = [q_hh(i);q_hl(i);q_ll(i);q_lh(i);q_hh(i)];
WallSupHeat_lim_TCC(:,i) = [WallSupHeat_h(i);WallSupHeat_l(i);WallSupHeat_l(i);↙
WallSupHeat_h(i);WallSupHeat_h(i)];
end


%% --- Uncalibrated Platinum RTD ---
tol_UCRTD = @(T) -0.003139*T + 1.441704;
limUCRTD = 1;
for i = limUCRTD:length(k)

tol_T1_UCRTD(i) = tol_UCRTD(T1(i));
tol_T2_UCRTD(i) = tol_UCRTD(T2(i));

T1_l(i) = T1(i)-tol_T1_UCRTD(i); T1_h(i) = T1(i)+tol_T1_UCRTD(i);
T2_l(i) = T2(i)-tol_T2_UCRTD(i); T2_h(i) = T2(i)+tol_T2_UCRTD(i);
```

```
WallSupHeat_h(i) = T2_h(i)-T_LN2;
WallSupHeat_l(i) = T2_l(i)-T_LN2;

% T1 high T2 high
h_hh(i) = 1/(r2*(T2_h(i)-T_LN2))*((k(i)*(T1_h(i)-T2_h(i)))/(log(r2/r1)));

% T1 hgih T2 low
h_hl(i) = 1/(r2*(T2_l(i)-T_LN2))*((k(i)*(T1_h(i)-T2_l(i)))/(log(r2/r1)));

% T1 low T2 high
h_lh(i) = 1/(r2*(T2_h(i)-T_LN2))*((k(i)*(T1_l(i)-T2_h(i)))/(log(r2/r1)));

% T1 low T2 low
h_ll(i) = 1/(r2*(T2_l(i)-T_LN2))*((k(i)*(T1_l(i)-T2_l(i)))/(log(r2/r1)));

q(i) = h(i)*(WallSupHeat(i));
q_hh(i) = h_hh(i)*(WallSupHeat_h(i));
q_hl(i) = h_hl(i)*(WallSupHeat_l(i));
q_lh(i) = h_lh(i)*(WallSupHeat_h(i));
q_ll(i) = h_ll(i)*(WallSupHeat_l(i));

q_lim_UC(:,i) = [q_hh(i);q_hl(i);q_ll(i);q_lh(i);q_hh(i)];
WallSupHeat_lim_UC(:,i) = [WallSupHeat_h(i);WallSupHeat_l(i);WallSupHeat_l(i);↙
WallSupHeat_h(i);WallSupHeat_h(i)];
end


%% --- Matched Platinum RTD ---

tol_MRTD = @(T) 0.00161816*T + -0.0044843;
limMRTD = 1;
for i = limMRTD:length(k)

tol_T1_MRTD(i) = tol_MRTD(T1(i));
tol_T2_MRTD(i) = tol_MRTD(T2(i));

T1_l(i) = T1(i)-tol_T1_MRTD(i); T1_h(i) = T1(i)+tol_T1_MRTD(i);
T2_l(i) = T2(i)-tol_T2_MRTD(i); T2_h(i) = T2(i)+tol_T2_MRTD(i);

WallSupHeat_h(i) = T2_h(i)-T_LN2;
WallSupHeat_l(i) = T2_l(i)-T_LN2;

% T1 high T2 high
h_hh(i) = 1/(r2*(T2_h(i)-T_LN2))*((k(i)*(T1_h(i)-T2_h(i)))/(log(r2/r1)));

% T1 hgih T2 low
h_hl(i) = 1/(r2*(T2_l(i)-T_LN2))*((k(i)*(T1_h(i)-T2_l(i)))/(log(r2/r1)));

% T1 low T2 high
h_lh(i) = 1/(r2*(T2_h(i)-T_LN2))*((k(i)*(T1_l(i)-T2_h(i)))/(log(r2/r1)));

% T1 low T2 low
h_ll(i) = 1/(r2*(T2_l(i)-T_LN2))*((k(i)*(T1_l(i)-T2_l(i)))/(log(r2/r1)));
```

```
q(i) = h(i)*(WallSupHeat(i));
q_hh(i) = h_hh(i)*(WallSupHeat_h(i));
q_hl(i) = h_hl(i)*(WallSupHeat_l(i));
q_lh(i) = h_lh(i)*(WallSupHeat_h(i));
q_ll(i) = h_ll(i)*(WallSupHeat_l(i));

q_lim_M(:,i) = [q_hh(i);q_hl(i);q_ll(i);q_lh(i);q_hh(i)];
WallSupHeat_lim_M(:,i) = [WallSupHeat_h(i);WallSupHeat_l(i);WallSupHeat_l(i);↙
WallSupHeat_h(i);WallSupHeat_h(i)];
end


%% --- SoftCal Platinum RTD ---
tol_SCRTD = 0.25;

limSCRTD = 1;
for i = limSCRTD:length(k)

tol_T1_SCRTD(i) = tol_SCRTD;
tol_T2_SCRTD(i) = tol_SCRTD;

T1_l(i) = T1(i)-tol_T1_SCRTD(i); T1_h(i) = T1(i)+tol_T1_SCRTD(i);
T2_l(i) = T2(i)-tol_T2_SCRTD(i); T2_h(i) = T2(i)+tol_T2_SCRTD(i);

WallSupHeat_h(i) = T2_h(i)-T_LN2;
WallSupHeat_l(i) = T2_l(i)-T_LN2;

% T1 high T2 high
h_hh(i) = 1/(r2*(T2_h(i)-T_LN2))*((k(i)*(T1_h(i)-T2_h(i)))/(log(r2/r1)));

% T1 hgih T2 low
h_hl(i) = 1/(r2*(T2_l(i)-T_LN2))*((k(i)*(T1_h(i)-T2_l(i)))/(log(r2/r1)));

% T1 low T2 high
h_lh(i) = 1/(r2*(T2_h(i)-T_LN2))*((k(i)*(T1_l(i)-T2_h(i)))/(log(r2/r1)));

% T1 low T2 low
h_ll(i) = 1/(r2*(T2_l(i)-T_LN2))*((k(i)*(T1_l(i)-T2_l(i)))/(log(r2/r1)));

q(i) = h(i)*(WallSupHeat(i));
q_hh(i) = h_hh(i)*(WallSupHeat_h(i));
q_hl(i) = h_hl(i)*(WallSupHeat_l(i));
q_lh(i) = h_lh(i)*(WallSupHeat_h(i));
q_ll(i) = h_ll(i)*(WallSupHeat_l(i));

q_lim_SC(:,i) = [q_hh(i);q_hl(i);q_ll(i);q_lh(i);q_hh(i)];
WallSupHeat_lim_SC(:,i) = [WallSupHeat_h(i);WallSupHeat_l(i);WallSupHeat_l(i);↙
WallSupHeat_h(i);WallSupHeat_h(i)];
end


%% --- Calibrated Platinum RTD ---
tol_CRTD = @(T) 0.000049327*T + 0.008201794;
```

```
limCRTD = 1;
for i = limCRTD:length(k)

tol_T1_CRTD(i) = tol_CRTD(T1(i));
tol_T2_CRTD(i) = tol_CRTD(T2(i));

T1_l(i) = T1(i)-tol_T1_CRTD(i); T1_h(i) = T1(i)+tol_T1_CRTD(i);
T2_l(i) = T2(i)-tol_T2_CRTD(i); T2_h(i) = T2(i)+tol_T2_CRTD(i);

WallSupHeat_h(i) = T2_h(i)-T_LN2;
WallSupHeat_l(i) = T2_l(i)-T_LN2;

% T1 high T2 high
h_hh(i) = 1/(r2*(T2_h(i)-T_LN2))*((k(i)*(T1_h(i)-T2_h(i)))/(log(r2/r1)));

% T1 hgih T2 low
h_hl(i) = 1/(r2*(T2_l(i)-T_LN2))*((k(i)*(T1_h(i)-T2_l(i)))/(log(r2/r1)));

% T1 low T2 high
h_lh(i) = 1/(r2*(T2_h(i)-T_LN2))*((k(i)*(T1_l(i)-T2_h(i)))/(log(r2/r1)));

% T1 low T2 low
h_ll(i) = 1/(r2*(T2_l(i)-T_LN2))*((k(i)*(T1_l(i)-T2_l(i)))/(log(r2/r1)));

q(i) = h(i)*(WallSupHeat(i));
q_hh(i) = h_hh(i)*(WallSupHeat_h(i));
q_hl(i) = h_hl(i)*(WallSupHeat_l(i));
q_lh(i) = h_lh(i)*(WallSupHeat_h(i));
q_ll(i) = h_ll(i)*(WallSupHeat_l(i));

q_lim_C(:,i) = [q_hh(i);q_hl(i);q_ll(i);q_lh(i);q_hh(i)];
WallSupHeat_lim_C(:,i) = [WallSupHeat_h(i);WallSupHeat_l(i);WallSupHeat_l(i);↙
WallSupHeat_h(i);WallSupHeat_h(i)];
end

%% --- SoftCal Platinum RTD - Matched ---
tol_SCMRTD = @(T) 0.0010762*T - 0.072869955;

limSCMRTD = 1;
for i = limSCMRTD:length(k)

tol_T1_SCMRTD(i) = tol_SCMRTD(T1(i));
tol_T2_SCMRTD(i) = tol_SCMRTD(T2(i));

T1_l(i) = T1(i)-tol_T1_SCMRTD(i); T1_h(i) = T1(i)+tol_T1_SCMRTD(i);
T2_l(i) = T2(i)-tol_T2_SCMRTD(i); T2_h(i) = T2(i)+tol_T2_SCMRTD(i);

WallSupHeat_h(i) = T2_h(i)-T_LN2;
WallSupHeat_l(i) = T2_l(i)-T_LN2;

% T1 high T2 high
h_hh(i) = 1/(r2*(T2_h(i)-T_LN2))*((k(i)*(T1_h(i)-T2_h(i)))/(log(r2/r1)));
```

```
% T1 hgih T2 low
h_hl(i) = 1/(r2*(T2_l(i)-T_LN2))*((k(i)*(T1_h(i)-T2_l(i)))/(log(r2/r1)));

% T1 low T2 high
h_lh(i) = 1/(r2*(T2_h(i)-T_LN2))*((k(i)*(T1_l(i)-T2_h(i)))/(log(r2/r1)));

% T1 low T2 low
h_ll(i) = 1/(r2*(T2_l(i)-T_LN2))*((k(i)*(T1_l(i)-T2_l(i)))/(log(r2/r1)));

q(i) = h(i)*(WallSupHeat(i));
q_hh(i) = h_hh(i)*(WallSupHeat_h(i));
q_hl(i) = h_hl(i)*(WallSupHeat_l(i));
q_lh(i) = h_lh(i)*(WallSupHeat_h(i));
q_ll(i) = h_ll(i)*(WallSupHeat_l(i));

q_lim_SCM(:,i) = [q_hh(i);q_hl(i);q_ll(i);q_lh(i);q_hh(i)];
WallSupHeat_lim_SCM(:,i) = [WallSupHeat_h(i);WallSupHeat_l(i);WallSupHeat_l(i);↙
WallSupHeat_h(i);WallSupHeat_h(i)];
end

%% --- Calibrated Platinum RTD - Matched ---
tol_CMRTD = @(T) 0.000058296*T + 0.005511211;

limCMRTD = 1;
for i = limCMRTD:length(k)

tol_T1_CMRTD(i) = tol_CMRTD(T1(i));
tol_T2_CMRTD(i) = tol_CMRTD(T2(i));

T1_l(i) = T1(i)-tol_T1_CMRTD(i); T1_h(i) = T1(i)+tol_T1_CMRTD(i);
T2_l(i) = T2(i)-tol_T2_CMRTD(i); T2_h(i) = T2(i)+tol_T2_CMRTD(i);

WallSupHeat_h(i) = T2_h(i)-T_LN2;
WallSupHeat_l(i) = T2_l(i)-T_LN2;

% T1 high T2 high
h_hh(i) = 1/(r2*(T2_h(i)-T_LN2))*((k(i)*(T1_h(i)-T2_h(i)))/(log(r2/r1)));

% T1 hgih T2 low
h_hl(i) = 1/(r2*(T2_l(i)-T_LN2))*((k(i)*(T1_h(i)-T2_l(i)))/(log(r2/r1)));

% T1 low T2 high
h_lh(i) = 1/(r2*(T2_h(i)-T_LN2))*((k(i)*(T1_l(i)-T2_h(i)))/(log(r2/r1)));

% T1 low T2 low
h_ll(i) = 1/(r2*(T2_l(i)-T_LN2))*((k(i)*(T1_l(i)-T2_l(i)))/(log(r2/r1)));

q(i) = h(i)*(WallSupHeat(i));
q_hh(i) = h_hh(i)*(WallSupHeat_h(i));
q_hl(i) = h_hl(i)*(WallSupHeat_l(i));
q_lh(i) = h_lh(i)*(WallSupHeat_h(i));
q_ll(i) = h_ll(i)*(WallSupHeat_l(i));

q_lim_CM(:,i) = [q_hh(i);q_hl(i);q_ll(i);q_lh(i);q_hh(i)];
```

```
WallSupHeat_lim_CM(:,i) = [WallSupHeat_h(i);WallSupHeat_l(i);WallSupHeat_l(i);
WallSupHeat_h(i);WallSupHeat_h(i)];
end

%% --- Plotting ---
figure(1)
loglog(WallSupHeat(:),q(:),'kx',WallSupHeat_lim_TC(:,:),q_lim_TC(:,:),'r',
WallSupHeat_lim_TCC(:,2),q_lim_TCC(:,2),'k',WallSupHeat_lim_UC(:,:),q_lim_UC
(:,:),'b',WallSupHeat_lim_M(:,:),q_lim_M(:,:),'m',WallSupHeat_lim_SC(:,:),q_lim_SC
(:,:),'g',WallSupHeat_lim_C(:,:),q_lim_C(:,:),'c')
ylim([3*10^3, 2*10^5]), xlim([6*10^-1, 1.75*10^1])
xlabel('T_w_a_l_l - T_s_a_t [K]'),ylabel('Heat Flux [W/m^2]'),title('Possible
Results for Different Sensor Types')
legend('Actual','Uncalibrated TC','','','','','','Calibrated
TC','','','','','','Uncalibrated RTD','','','','','','Matched
RTD','','','','','','SoftCal RTD','','','','','','Calibrated
RTD','location','northwest')

figure(2)
plot(WallSupHeat(2),q(2),'kx',WallSupHeat_lim_TC(:,2),q_lim_TC(:,2),'r',
WallSupHeat_lim_TCC(:,2),q_lim_TCC(:,2),'k',WallSupHeat_lim_UC(:,2),q_lim_UC(:,
2),'b',WallSupHeat_lim_M(:,2),q_lim_M(:,2),'m',WallSupHeat_lim_SC(:,2),q_lim_SC(:,
2),'g',WallSupHeat_lim_C(:,2),q_lim_C(:,2),'c')
ylim([2.5*10^4, 3.1*10^4]), xlim([2*10^0, 8.2*10^0])
xlabel('T_w_a_l_l - T_s_a_t [K]'),ylabel('Heat Flux [W/m^2]'),title('Possible
Results for Different Sensor Types at 5.1 K Wall Heat')
legend('Actual','Uncalibrated TC','Calibrated TC','Uncalibrated RTD','Matched
RTD','SoftCal RTD','Calibrated RTD','location','southwest')

figure(3)
plot(WallSupHeat(2),q(2),'kx',WallSupHeat_lim_TCC(:,2),q_lim_TCC(:,2),'k',
WallSupHeat_lim_M(:,2),q_lim_M(:,2),'m',WallSupHeat_lim_SC(:,2),q_lim_SC(:,2),'g',
WallSupHeat_lim_C(:,2),q_lim_C(:,2),'c')
ylim([27800, 28362]), xlim([4.8, 5.4])
xlabel('T_w_a_l_l - T_s_a_t [K]'),ylabel('Heat Flux [W/m^2]'),title('Possible
Results for Calibrated Types at 5.1 K Wall Heat')
legend('Actual','Calibrated TC','Matched RTD','SoftCal RTD','Calibrated
RTD','location','southwest')

%% --- Comparing Cost and Tol ---
d_TC=sqrt((q_lim_TC(2,2)-q_lim_TC(4,2))^2+(WallSupHeat_lim_TC(2,2)-
WallSupHeat_lim_TC(4,2))^2);
d_UC=sqrt((q_lim_UC(2,2)-q_lim_UC(4,2))^2+(WallSupHeat_lim_UC(2,2)-
WallSupHeat_lim_UC(4,2))^2);
d_SC=sqrt((q_lim_SC(2,2)-q_lim_SC(4,2))^2+(WallSupHeat_lim_SC(2,2)-
WallSupHeat_lim_SC(4,2))^2);
d_M=sqrt((q_lim_M(2,2)-q_lim_M(4,2))^2+(WallSupHeat_lim_M(2,2)-WallSupHeat_lim_M
(4,2))^2);
d_TCC=sqrt((q_lim_TCC(2,2)-q_lim_TCC(4,2))^2+(WallSupHeat_lim_TCC(2,2)-
WallSupHeat_lim_TCC(4,2))^2);
d_SCM=sqrt((q_lim_SCM(2,2)-q_lim_SCM(4,2))^2+(WallSupHeat_lim_SCM(2,2)-
WallSupHeat_lim_SCM(4,2))^2);
d_C=sqrt((q_lim_C(2,2)-q_lim_C(4,2))^2+(WallSupHeat_lim_C(2,2)-WallSupHeat_lim_C
(4,2))^2);
```

```
d_CM=sqrt((q_lim_CM(2,2)-q_lim_CM(4,2))^2+(WallSupHeat_lim_CM(2,2)-↙
WallSupHeat_lim_CM(4,2))^2);

figure(4)
semilogy(61.68,d_TC,'rx',169,d_UC,'bx',360,d_SC,'gx',419,d_M,'mx',150,d_TCC,'kx',↙
431,d_SCM,'go',621,d_C,'cx',691,d_CM,'co')
title('Cost vs Tolerance Comparison'),xlabel('Cost [$]'),ylabel('Characteristic↙
Tolerance [W/m^2]')
legend('TC ($62)','Uncalibrated RTD ($170)','SoftCal ($360)','Matched↙
($419)','Calibrated TC ($150)','Matched SoftCal ($431)','Calibrated RTD↙
($621)','Matched Calibrated RTD ($691)','Location','southwest')
```